AIAA Propulsion and Energy Forum
10-12 July 2017, Atlanta, GA
53rd AIAA/SAE/ASEE Joint Propulsion Conference

10.2514/6.2017-4918



# Reduced-Order Reconstruction of Model Rocket Combustor Flows

Xu, Jiayang*and Karthik Duraisamy†
*University of Michigan, Ann Arbor, Michigan, 48109, U.S.A.*

**This work reports preliminary results on the application of projection-based reduced-order models (ROMs) to the study of combustion dynamics in liquid-fueled rocket engines. Specifically, quasi-one-dimensional and axisymmetric (two-dimensional) models of a single element rocket combustor are explored. In the one-dimensional case, a POD-Galerkin-based ROM is shown to accurately reproduce the evolution of pressure perturbations over a wide region in parameter space. Next, the viability of sampling/interpolation techniques in accelerating ROM solutions is explored. Three techniques - the discrete empirical interpolation method (DEIM), a QR decomposition-based DEIM (QDEIM) and an adaptive technique (ADEIM) are used to reconstruct the solution in the entire domain based on sparse samples. All three techniques are shown to yield a low reconstruction error based on a very small fraction of sampling points ($< 1\%$ for the axisymmetric case). The ADEIM, by virtue of dynamically adapting the basis functions and sampling points, is seen to reduce the reconstruction error considerably in comparison to the DEIM/QDEIM, suggesting its viability in predictive ROMs of realistic rocket combustors.**



## I. Introduction

The design of liquid rocket engines (LREs) is complicated by the presence of combustion instabilities. These instabilities are characterized by the coupling between high-amplitude pressure waves, heat release, and hydrodynamics. Combustion instabilities (CI) have long been recognized as critical to rocket design and have led to several catastrophic failures in the development of rocket engines including the B-1 engine in Atlas D rocket[1] and the Saturn F-1 engine.[2] Even though the underlying phenomena have been understood from a phenomenological perspective, CI continues to be a hurdle in the development of modern rocket engines. The phenomena is intrinsically self-excited due to the acoustic properties within the combustion chamber as well as the additional coupling between hydrodynamics, flame dynamics and heat release.[3] Thus, the problem is sensitive to the engine geometry and reactant properties, requiring evaluations of the performance on numerous combinations of parameters in the research and development process.

Theoretical analysis of LRE combustion instabilities have been proposed since 1940s.[4–7] While analytic approaches provide the necessary insight, the complexity of the problem renders the accuracy of simplified models to be limited to the confines of the model calibration. High-fidelity numerical simulation methods including Direct numerical simulations (DNS) large eddy simulations (LES) and hybrid Reynolds-averaged Navier–Stokes/LES (RANS/LES) have been proven their viability in predicting generic combustion process.[8–10] Even hybrid RANS/LES will be prohibitively expensive for application in full-scale rocket engines in the decades to come. The demand for practical predictive methods or design purposes, thus encourages the recent explorations in low-complexity models.

Commonly adopted simplifications in reduced-fidelity models include reduced chemical reaction mechanisms[11–13] and low-dimension approximation.[12,14] Although failing to predict finer details of the flow, these methods can often be tuned for specific problems and provide satisfying accuracy in critical properties such as pressure, velocity and heat release for LRE modeling. However, the tuning process is typically empirical and iterative, involving calibration based on experiment or high-fidelity simulation data. In recent years, modal decomposition techniques have been applied to high-resolution experimental data to extract low-order

*Graduate Student Research Assistant, Aerospace Engineering Department, davidxu@umich.edu.
†Associate Professor, Aerospace Engineering Department, kdur@umich.edu.

representations of the combustion dynamics.[15,16] Their successes illustrate the potential of applying reduced order methods to efficiently account for the underlying dynamics.

With a vision of developing predictive reduced order models of LREs, this work reports preliminary results on the application of projection-based reduced-order models (ROM) to a single element model rocket combustor. Specifically, quasi-one-dimensional and axisymmetric (two-dimensional) versions of the continuous variable resonance combustor (CVRC)[17,18] are considered.

In Sec. II, the quasi-1D CVRC setup is introduced. The full-order model and results are described in Sec. III. The projection-based reduced-order model and results are presented and in Sec. IV. With a view towards ROM development for realistic configurations, the possibility of achieving acceleration with sparse sampling is discussed in Sec. V. The results from sparse sampling-based reconstruction are presented and analyzed in Sec. VI. Concluding remarks are given in Sec. VII

## II. Quasi-1D CVRC setup

Initial studies are performed on a quasi one-dimensional version of the CVRC. The idealized computational domain is sketched in Fig. 1, with geometry parameters given in Table 1. The CVRC is a singe element model rocket combustor characterized by a continuously variable oxidizer injector tube serving as a wave resonator, designed for the study of longitudinal combustion instabilities.[17,18] The fuel is injected through an annular ring around the oxidizer injector, located at the back-step shown in Fig. 1. Both the injector and the nozzle are operated at choked condition during the experiment. To avoid invalidating the quasi-one-dimensional equations, the step and the converging part of the nozzle are sinusoidally contoured in this study (in contrast to a discontinuous cross-sectional area change in the real setup).

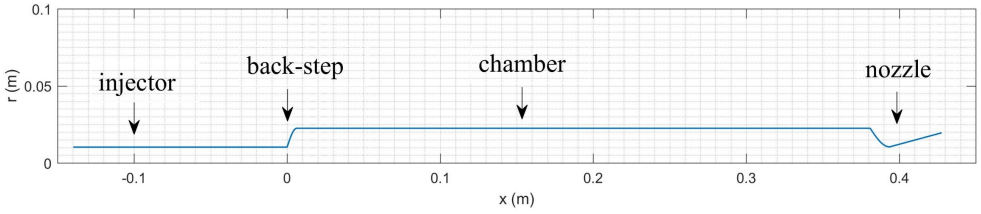


Figure 1: Computational domain

| Section | Injector | Back-step | Chamber | Converging Section | Nozzle |
|---|---|---|---|---|---|
| Length (cm) | 13.97 | 1.27 | 63.5 | 1.27 | 7.62 |
| Radius (cm) | 1.12 | 1.12 2.25 | 2.25 | 2.25 1.08 | 1.08 1.33 |

Table 1: Geometry parameters

Propellants are methane and hydrogen peroxide (more precisely 90% $H_2O_2$ and 10% $H_2O$), with the operating conditions given in Table 2.

## III. Full-order system

### A. Governing equations

The governing equations are given in Eq. (1), and are based on previous studies[19,20] with some modifications.

$$\frac{\partial \mathbf{q}}{\partial t} + \frac{\partial \mathbf{f}}{\partial x} = \mathbf{s} + \mathbf{s}_f + \mathbf{s}_q, \tag{1}$$

| Parameter | Value |
|---|---|
| Fuel Mass Flow Rate, kg/s | 0.027 |
| Fuel Temperature, K | 300 |
| Oxidizer Mass Flow Rate, kg/s | 0.32 |
| Oxidizer Temperature, K | 1030 |
| Mass Fraction $H_2O$, % | 57.6 |
| Mass Fraction $O_2$, % | 42.4 |
| Equivalence Ratio | 0.8 |

Table 2: CVRC Operating conditions

where

$$\mathbf{q} = \begin{pmatrix} \rho \\ \rho u \\ E_0 \\ \rho Y_{ox} \end{pmatrix}; \mathbf{f} = \begin{pmatrix} \rho u \\ \rho u^2 + p \\ E_0 + p \\ \rho u Y_{ox} \end{pmatrix}; \mathbf{s} = \begin{pmatrix} 0 \\ \frac{p}{A}\frac{dA}{dx} \\ 0 \\ 0 \end{pmatrix}; \mathbf{s}_f = \begin{pmatrix} \dot{\omega}_f \\ \dot{\omega}_f u \\ \dot{\omega}_f \Delta h_0 \\ -\dot{\omega}_{ox} \end{pmatrix}; \mathbf{s}_q = \begin{pmatrix} 0 \\ 0 \\ q' \\ 0 \end{pmatrix}, \tag{2}$$

and $Y_{ox}$ is the oxidizer mass fraction.

The first source term, $\mathbf{s}$, is due to area variations while the other two terms are related to combustion. An important assumption made here is that fuel reacts instantaneously to form products with the main consequence of neglecting intermediate species and finite reaction rates. To avoid discontinuities and to reproduce a combustion region of finite length, fuel is injected through a region after the back-step, between $l_s = -0.0063\ m$ and $l_f = 0.0699\ m$ with a sinusoidal shape, yielding

$$\dot{\omega}_f = \frac{\dot{m}_f}{A \int (1 + \sin\xi) dx} (1 + \sin\xi), \tag{3}$$

$$\dot{\omega}_{ox} = \dot{\omega}_f / C_{f/o}, \tag{4}$$

with

$$\xi = -\frac{\pi}{2} + 2\pi \frac{x - l_s}{l_f - l_s}, \text{with } l_s < x < l_f. \tag{5}$$

The last contribution, $\mathbf{s}_q$, refers to the unsteady heat release term. It represents the response function, through which the model takes into account coupling between acoustics and combustion. Expressing the unsteady part of the heat release as a function of pressure with an amplification parameter $\alpha$ and a time lag $\tau$,

$$q' = \dot{\omega}_f \Delta h_0 \alpha \frac{p(x, t - \tau) - \bar{p}(x)}{\bar{p}(x)}. \tag{6}$$

An upwind finite volume discretization is employed with explicit time stepping using the fourth-order Runge Kutta (RK4) scheme. 1200 control volumes were required to assure grid convergence. The full-order result is briefly presented in the following section to verify the solver.

### B. Steady state solutions

The steady state solution is first obtained by turning off the unsteady source term, $S_q$. Pressure and temperature are plotted in Fig. 2, which are identical to the result from Ref. 20.

### C. Unsteady results

In unsteady simulations, the choice of parameters is $\alpha = 3.6, \tau = T, \Delta t = 1.64 \times 10^{-7}$ s, where $T$ is the time period associated with the analytical first longitudinal resonant frequency (1400 Hz).[19] To excite pressure oscillations, a small amplitude disturbance is applied to the mass flow rate until a limit cycle is established. The unsteadiness is evaluated using pressure signals obtained at 36.8 cm behind the oxidizer injector. The choice of this point is related to the availability of a pressure probe at this location in the experimental test.[19]

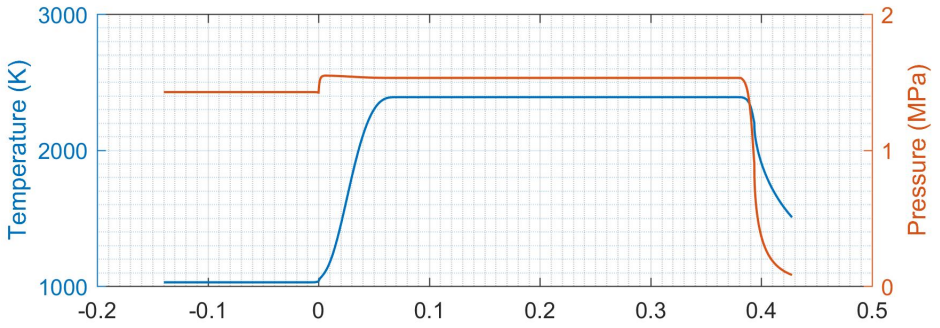


Figure 2: Steady state pressure and temperature



The history of the pressure oscillation and its power spectral density (PSD) is presented in Fig. 3, which shows consistency with experimental results.[3] A comparison between the computed and experimental longitudinal frequencies is given in Table 3 where the error is below 2%. It should be noted that the choice of $\tau$ only determines the growth of instability together with $\alpha$, but does not directly affect the computed frequency.

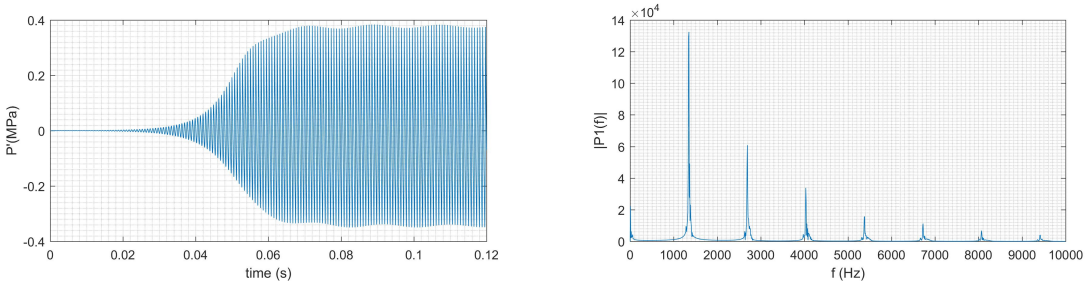


(a) Pressure oscillation history

(b) Single-sided amplitude spectrum

Figure 3: Full-order unsteady state result

| Mode | 1L | 2L | 3L |
|---|---|---|---|
| $f_{exp}$ (Hz) | 1330 | 2660 | 3990 |
| $f_{comp}$ (Hz) | 1350 | 2692 | 4034 |

Table 3: Comparison between computed and experimental longitudinal frequencies

## IV. Projection-based reduced-order modeling

In the context of configurations of interest to this paper, different approaches have been taken towards reduced complexity models in prior studies. Most of these works are based on empirical relations[21] or local linearity assumptions,[22,23] which limit these methods within the proximity of the training data. We will pursue projection-based model reduction techniques[24,25] as these techniques have shown promise in describing nonlinear dynamics with moving shocks.[26–28] An introduction to POD/Galerkin method to fluid flows can be found in Ref. 24.

### A. ROM implementation

The first step in POD projection-based reduced-order modeling is to develop a reduced basis. This can be achieved using the singular value decomposition (SVD),[29] the left singular vectors of which minimize

the Frobenius norm of the projection error. Taking $\mathbf{A}$ as a data matrix consisting of solution "snapshots" aligned in columns, the SVD is given by

$$\mathbf{A} = \mathbf{U}\mathbf{\Sigma}\mathbf{V}^*. \tag{7}$$

Each column of $\mathbf{U}$ can be used as part of an orthonormal basis set. $\mathbf{\Sigma}$ is a diagonal matrix whose diagonal elements are singular values of $\mathbf{A}$, arranged in descending order. The singular values can be used to judge the norm of the projection error for a given set of basis functions.

To derive the ROM equations, we first rewrite Eq. (1) as

$$\frac{d\mathbf{q}}{dt} = \mathbf{r}\left(\mathbf{q}\left(x,t\right)\right), \tag{8}$$

where the residual vector

$$\mathbf{r} = -\frac{\partial \mathbf{f}}{\partial x} + \mathbf{s} + \mathbf{s_f} + \mathbf{s_q}. \tag{9}$$

At each time-step in FOM, the solution of $\mathbf{q} \in \mathbb{R}^n$ at all grid points is stored in a single column. These stored solutions form a snapshot matrix $\mathbf{Q}_{snap} \in \mathbb{R}^{n \times n_t}$. From the SVD, we have $\mathbf{Q}_{snap} = \mathbf{U}\mathbf{\Sigma}\mathbf{V}^*$. Assuming $m_L$ is the dimension of the resolved modes, the approximated solution is

$$\mathbf{q} \approx \tilde{\mathbf{q}} = \mathbf{\Phi}\mathbf{q}_r\left(t\right), \tag{10}$$

where $\mathbf{\Phi} = \mathbf{U}_{1:m_L}$ is the spatial basis matrix of $\mathbf{Q}_{snap}$, and $\mathbf{q}_r$ is the $m_L$-dimensional reduced-order variable.

Then the truncated Galerkin-ROM equation of Eq. (8) is

$$\frac{d\tilde{\mathbf{q}}}{dt} = \mathbf{\Phi}^T\mathbf{r}\left(\mathbf{\Phi}\mathbf{q}_r\right). \tag{11}$$

### B. ROM results

In this study, the snapshots are obtained every 100 time steps over the first 0.1 second of the FOM evolution. Table 4 shows the number of modes required to represent the fraction of energy for each of the four variables $(\rho, \rho u, E_0, \rho Y_{ox})$, calculated from (12) for each mode.

$$\eta_i = \frac{\sigma_i}{\sum_{j=1}^{n} \sigma_j}, \tag{12}$$

where $\sigma_i$ is the corresponding singular values of the $i$-th mode. The 100 leading modes are presented in Fig. 4. Due to the relatively slow decay in the singular value spectrum, 151 out of 1200 modes in the ROM for each variable are retained for the computation.

| Property | 90% | 95% | 99% |
|---|---|---|---|
| $\rho$ | 16 | 35 | 92 |
| $\rho u$ | 33 | 56 | 114 |
| $E_0$ | 13 | 30 | 87 |
| $\rho Y_{ox}$ | 14 | 31 | 82 |

Table 4: Energy content as a function of number of modes retained.

To evaluate the performance of the ROM over a wide range of states, the ROM is initialized from the steady state result (Sec. III.C). This requires the ROM to capture the growth of the perturbations and transition from stable to unstable states. With less than 13% modes retained, the ROM demonstrates an ability to retain accuracy and stability with time steps corresponding to CFL numbers up to 5, which is an indication of better conditioning of the ROM compared to the FOM.

A comparison of the time history of the pressure for different CFL numbers is given in Fig. 5(a)-5(c). In comparison, Fig. 5(d) shows the result when the ROM is appended to the FOM after limit cycle oscillations are established. The transition point displayed in the zoomed-in view (the two cycles before $t = 0.1$ s are FOM). The error in the solution is listed in Table 5, which is measured from Eq. (13). It is interesting to note

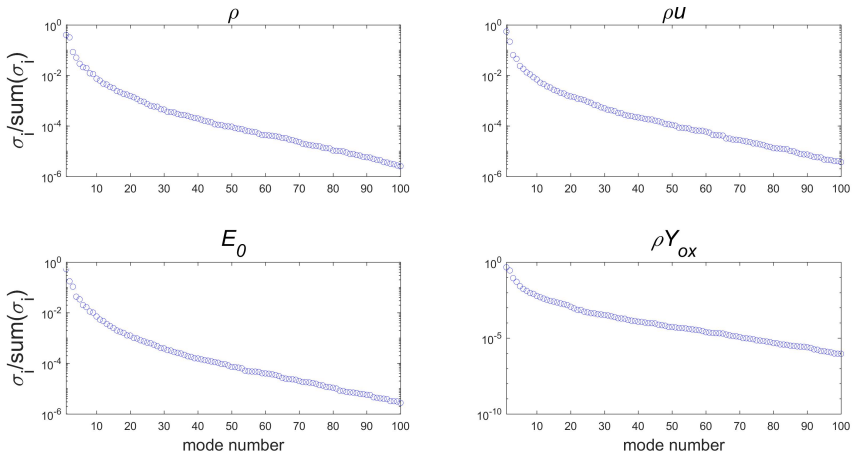


Figure 4: Leading singular values for different variables

that a lower CFL number does not necessarily lead to a lower error, potentially suggesting the complicated nature of the truncated terms.

$$e = \frac{\|\mathcal{S}_F - \mathcal{S}_R\|_2}{\|\mathcal{S}_F\|_2}, \tag{13}$$

where $\mathcal{S}_F$ and $\mathcal{S}_R$ is the full-order with CFL = 1 and reduced-order solution history at the monitored point.

| | restarted | | | appended |
|---|---|---|---|---|
| CFL | 1 | 3 | 5 | 1 |
| error (%) | 2.16 | 1.60 | 1.88 | 1.19 |

Table 5: Error in ROM solution

Fig. 6 shows the evolution of the pressure perturbations. In the context of combustor instabilities, an important property to be evaluated is the growth rate of the pressure oscillation (defined in Fig. 7) after the perturbation in inlet is imposed. A positive growth rate implies a growing instability.

A comparison of the growth rate from the FOM and ROM computations is given in Fig. 8, where the injector/chamber length ($L_i/L_c$) and the amplification parameter, $\alpha$ are used as variables. The ROM is seen to accurately reconstruct the correct growth rate in all cases.

## V. Prospects for acceleration using sparse sampling

Eq. (11) represents a non-intrusive formulation, in which the internal details of the residual operator are not required to compute the ROM solution. However, even though $\tilde{\mathbf{q}} \in \mathbb{R}^{m_L}$, the evaluation of the residual $\mathbf{r} \in \mathbb{R}^n$ still requires $O(n)$ evaluations. Thus, the efficiency gains of non-intrusive POD-based ROMs at each time-step may be limited and the acceleration may be achieved courtesy of the decreased stiffness of the ROM compared to the FOM. Sparse sampling[30] or hyper-reduction[25] techniques - on the other hand - allow for the processing of the ROM based on the evaluation of the residual at a few critical points.

### A. Sparse sampling with discrete empirical interpolation method[30]

Assuming snapshots $\mathbf{M}$ of the residual $\mathbf{r}$ can be obtained, a POD basis $\mathbf{\Psi} \in\in \mathbb{R}^{n\times m_L}$ can be built and an approximation of the residual can be developed $\mathbf{r} \approx \tilde{\mathbf{r}} = \mathbf{\Psi c}$, where $\mathbf{c} \in \mathbb{R}^{m_L}$ are basis coefficients.

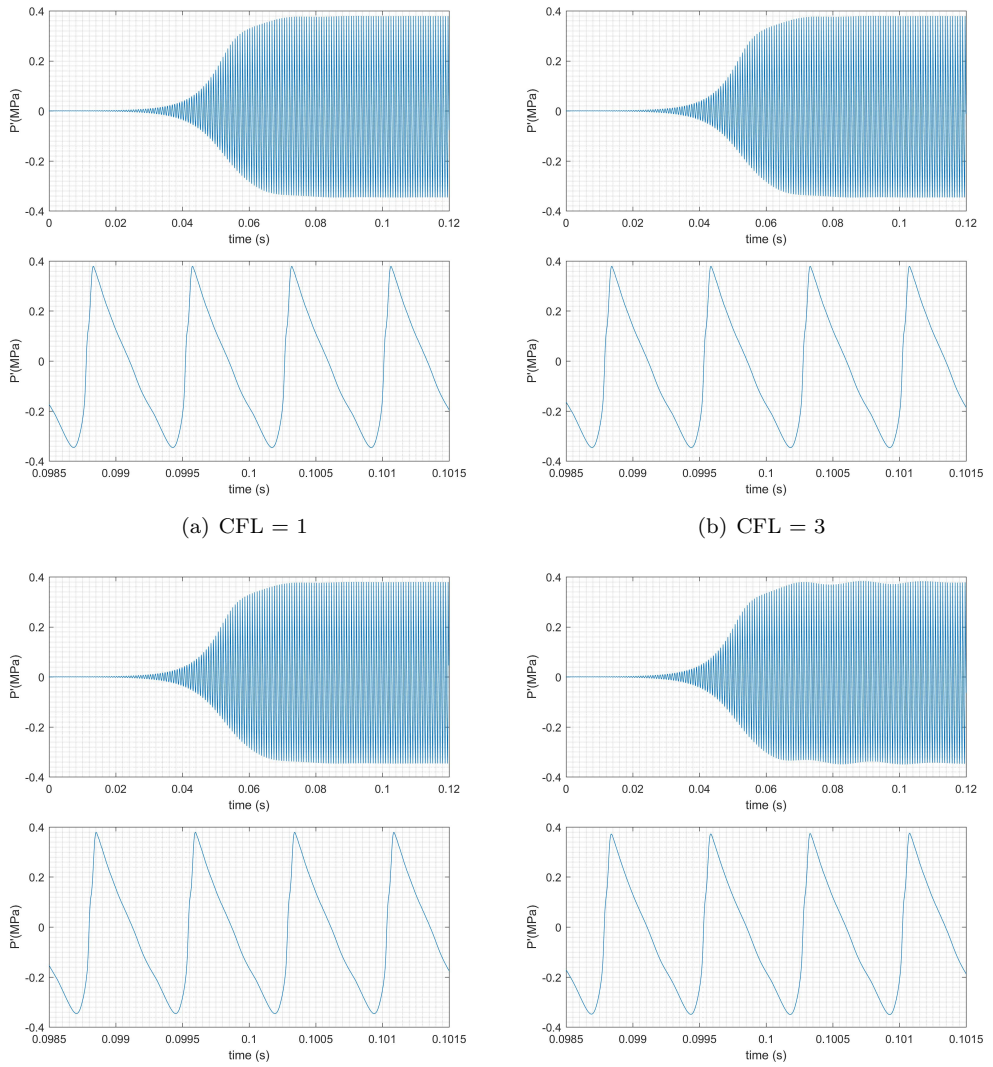


(a) CFL = 1

(b) CFL = 3

(c) CFL = 5

(d) FOM (0 ∼ 0.1s)-ROM (0.1 ∼ 0.12s), CFL = 1

Figure 5: Reduced-order result for pressure oscillation with zoomed-in views

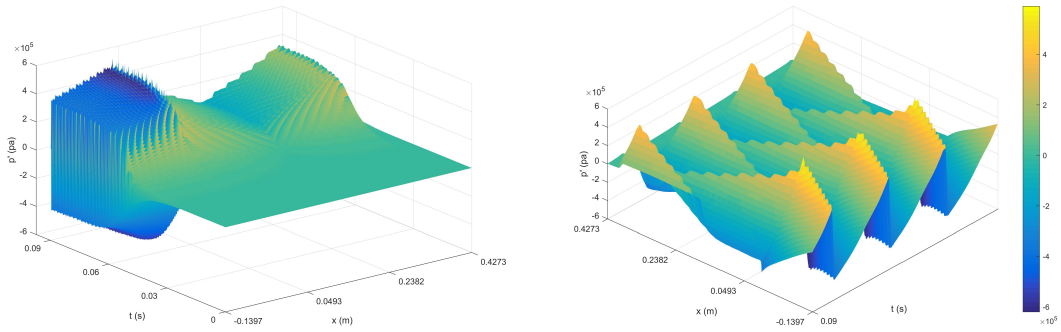


(a) Spatial pressure profile for $t = 0 \sim 0.1s$

(b) Zoomed-in view for 4 cycles

Figure 6: Pressure oscillation growth profile

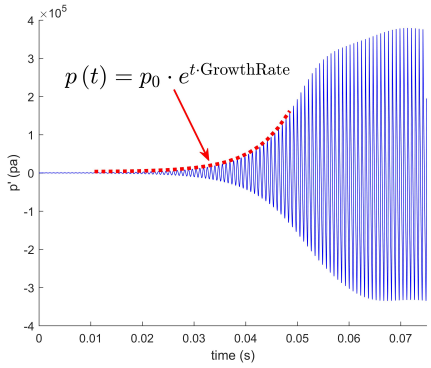


Figure 7: Definition of Growth Rate

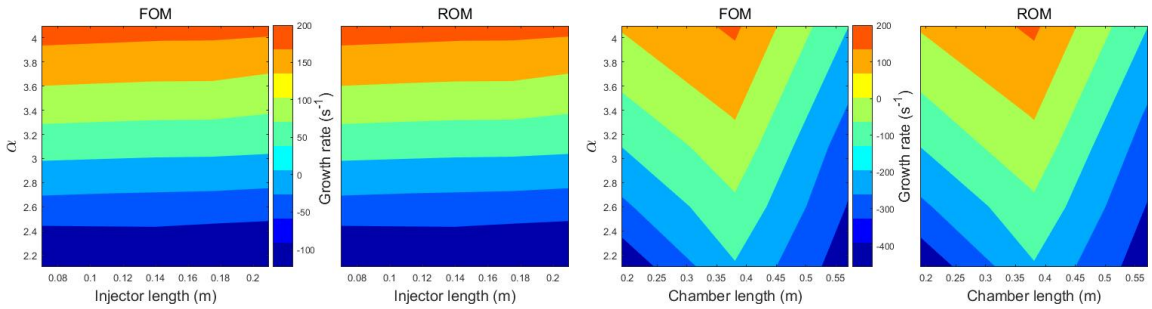


(a) Variate $L_i$ with $L_c = 0.38$m

(b) Variate $L_c$ with $L_i = 0.14$m

Figure 8: Growth rate comparison

Introducing a sample selection matrix $\mathbf{P} \in \mathbb{R}^{n \times m_L}$ that selects $m_L$ locations $\hat{x}_i$:

$$P_{ij} = \begin{cases} 1 & \hat{x}_i = x_j \\ 0 & \text{elsewhere} \end{cases}.$$

It is easy to see that $\mathbf{P}\tilde{\mathbf{r}} = \mathbf{P}\boldsymbol{\Psi}\mathbf{c}$. Hence,

$$\tilde{\mathbf{r}} = \boldsymbol{\Psi}\left(\mathbf{P}\boldsymbol{\Psi}\right)^{-1}\mathbf{P}\mathbf{r}. \tag{14}$$

Thus $\tilde{\mathbf{r}}$ is an approximation to $\mathbf{r}$ based on samples $\mathbf{P}\mathbf{r}$.

The critical points, $\hat{\mathbf{x}}$, can be chosen using a number of techniques. The discrete empirical interpolation method (DEIM)[30] is perhaps the most widely adopted. DEIM utilizes the dominant features extracted from POD to determine the optimized sampling points for the dynamic modes of interest. Given a basis $\boldsymbol{\Psi}$, the idea then is to find a sensor selection matrix $\mathbf{P}^*$ that minimizes the difference between the real and reconstructed signal. In other words,

$$\mathbf{P}^* = \min_{\mathbf{P}} \left\| \mathbf{M} - \boldsymbol{\Psi}[\mathbf{P}\boldsymbol{\Psi}]^{+}\hat{\mathbf{M}} \right\|_2, \tag{15}$$

where $\hat{\mathbf{M}} = \mathbf{P}\mathbf{M}$ denotes the measured residual at the sensors selected by $\mathbf{P}$. In popular approaches, the number of sensors is set to $m_L$ and $\mathbf{P}^*$ is chosen as

$$\mathbf{P}^* = \min_{\mathbf{P}} \left\| \mathbf{M} - \boldsymbol{\Psi}[\mathbf{P}\boldsymbol{\Psi}]^{-1}\hat{\mathbf{M}} \right\|_2. \tag{16}$$

It is easily shown (Ref. 31, for instance) that

$$\left\| \mathbf{M} - \boldsymbol{\Psi}[\mathbf{P}\boldsymbol{\Psi}]^{-1}\mathbf{P}\mathbf{M} \right\|_2 \leq \left\| [\mathbf{P}\boldsymbol{\Psi}]^{-1} \right\|_2 \left\| \left[\mathbf{I} - \boldsymbol{\Psi}\boldsymbol{\Psi}^T\right]\mathbf{M} \right\|_2. \tag{17}$$

The second term in the RHS of Eqn. (17) is projection error, and hence the first term can be considered sampling error. Thus DEIM-based approaches simplify the sensor selection problem to

$$\mathbf{P}^* = \min_{\mathbf{P}} \left\| [\mathbf{P}\boldsymbol{\Psi}]^{-1} \right\|_2. \tag{18}$$

The determination of the sensor locations is given in Algorithm 1, where $\hat{\mathbf{x}}$ denotes the sampling points selected by $\mathbf{P}^*$.

**Algorithm 1** Discrete empirical interpolation method

**Input:** $\boldsymbol{\Psi}_{n\times n_L} = [\psi_1, \ldots, \psi_{m_L}]$
**Output:** $\hat{\mathbf{x}} = [\hat{x}_1, \ldots \hat{x}_{m_L}]$
  $[\rho, \hat{x}_1] = \max(|\psi_1|)$
  $\hat{\mathbf{x}} = [\hat{x}]$
  **for** $i = 2$ **to** $m_L$ **do**
    $\phi \leftarrow \psi_i$
    Solve $\boldsymbol{\Psi}_{\hat{\mathbf{x}}}\mathbf{c} = \phi_{\hat{\mathbf{x}}}$ for $\mathbf{c}$
    $\varepsilon = \phi - \boldsymbol{\Psi}\mathbf{c}$
    $[\rho, \hat{x}_i] = \max(|\varepsilon|)$
    $\hat{\mathbf{x}} = [\hat{\mathbf{x}}, x_i]$
  **end for**

### B. QR decomposition-based DEIM (QDEIM)

An elegant way of approaching the sensor selection problem is the QDEIM[32,33] method which relies on rank revealing QR decomposition (RRQR)[34–36] with column pivoting. The RRQR pivoting for $\boldsymbol{\Psi}^T$ can be expressed as

$$\boldsymbol{\Psi}^T\boldsymbol{\Pi} = \mathbf{Q}\mathbf{R}, \tag{19}$$

where $\boldsymbol{\Pi}$ is the column permutation matrix. It should be noted that any sample selection matrix $\mathbf{P}_1$ for $\boldsymbol{\Psi}$ can be constructed from rows of $\boldsymbol{\Pi}^T$. Thus Eq. (19) can be converted and separated into

$$\begin{bmatrix} \mathbf{P}_1 \\ \mathbf{P}_2 \end{bmatrix} \boldsymbol{\Psi} = \begin{bmatrix} \mathbf{R}_1^T \\ \mathbf{R}_2^T \end{bmatrix} \mathbf{Q}^T, \tag{20}$$

where $\mathbf{P}_2$ denotes the rest of $\boldsymbol{\Pi}^T$ after removing $\mathbf{P}_1$. Because $\mathbf{Q}$ is an orthogonal matrix, we have

$$\left\|\mathbf{P}_1^T\boldsymbol{\Psi}\right\|_2 = \left\|\mathbf{R}_1^T\mathbf{Q}^T\right\|_2 = \|\mathbf{R}_1\|_2 = \sigma_{\max}(\mathbf{R}_1), \tag{21}$$

and

$$\left\| \left(\mathbf{P}_1^T\boldsymbol{\Psi}\right)^{-1} \right\|_2 = \frac{1}{\sigma_{\min}(\mathbf{R}_1)}. \tag{22}$$

Thus the minimization problem in Eq. (18) can be solved by keeping $\sigma_{\min}(\mathbf{R}_1)$ as large as possible, which is accomplished by RRQR.[35,36] Therefore as suggested in Ref. 33, we can set $\mathbf{P}_1$ to the leading rows of $\boldsymbol{\Pi}^T$. In other words, a solution to Eq. (18) is

$$\mathbf{P}^* = \boldsymbol{\Pi}^T_{:,1:m_L}. \tag{23}$$

### C. Adaptive DEIM

The sampling points as well as the basis functions used in the DEIM/QDEIM are fixed for the entire simulation. This may not necessarily be optimal in applications such as the rocket combustor, in which the flow can undergo rapid topological changes. Further, difficulties in accounting for propagating waves using fixed basis functions has been well-recognized.[37] This has lead to the development of methods such as the adaptive DEIM (ADEIM).[38]

At each time step (subscript k), the ADEIM technique randomly picks $m_S$ additional sampling points and generates an intermediate measurement matrix, $\mathbf{S}_k$, corresponding to the $(m + m_S)$ sampling points.

Instead of solving for the optimal choice of measurement matrix as in Eqn. (18), ADEIM seeks an optimal update to the basis using the following minimization problem

$$\underset{\alpha_k \in \mathbb{R}^n, \beta_k \in \mathbb{R}^m}{\arg\min} \left\| \mathbf{S}_k^T \mathbf{E}_k + \mathbf{S}_k^T \alpha \beta^T \mathbf{c}_k \right\|_F^2, \tag{24}$$

where is $\mathbf{c}_k$ is the coefficient matrix for the basis $\mathbf{\Psi}_{k-1}$, $\mathbf{E}_k = \mathbf{\Psi}_{k-1}\mathbf{c}_k - \mathbf{M}_k$ is the residual matrix, and $\alpha\beta^T$ represents an update to the basis

$$\mathbf{\Psi}_k = \mathbf{\Psi}_{k-1} + \alpha_k \beta_k^T. \tag{25}$$

In Ref. 38 it is shown that if $\left\| \mathbf{S}_k^T \mathbf{E}_k \mathbf{c}_k^T \right\|_F = 0$, an optimal update $\alpha_k \beta_k^T$ with respect to Eqn. (24) is $\alpha_k = \mathbf{0}_n \in \mathbb{R}^n$ and $\beta_k = \mathbf{0}_w \in \mathbb{R}^w$, where $\mathbf{0}_n$ and $\mathbf{0}_w$ are the n- and w-dimensional null vectors respectively; and that when $\left\| \mathbf{S}_k^T \mathbf{E}_k \mathbf{c}_k^T \right\|_F > 0$, an optimal update is given by setting

$$\begin{aligned} \alpha_k &= \mathbf{S}_k \alpha_k^{'}, \\ \beta_k &= \mathbf{Q}_k \beta_k^{'}, \end{aligned} \tag{26}$$

where $\mathbf{Q}_k$ is from a rank-revealing QR decomposition $\mathbf{c}_k = \mathbf{Q}_k \mathbf{Z}_k$, $\beta_k^{'} \in \mathbb{R}^m$ is an eigenvector corresponding to the largest eigenvalue $\lambda \in \mathbb{R}$ of the generalized eigenvalue problem $\mathbf{c}_k \left(\mathbf{S}_k^T \mathbf{E}_k\right)^T \left(\mathbf{S}_k^T \mathbf{E}_k\right) \mathbf{c}_k^T \beta_k^{'} = \lambda \mathbf{c}_k \mathbf{c}_k^T \beta_k^{'}$, and $\alpha_k^{'} = -1 / \left\| \mathbf{c}_k^T \beta_k^{'} \right\|_2^2 \mathbf{S}_k^T \mathbf{E}_k \mathbf{c}_k^T \beta_k^{'}$.

After the basis is updated using Eqn. (25), sampling points are then re-evaluated based on the updated basis.[38]

## VI. Results from sparse sampling-based reconstruction

To make an initial assessment of the viability of sparse sampling methods, the pressure field from one- and two-dimensional versions of the CVRC is reconstructed using the DEIM/QDEIM/ADEIM.

### A. 1D results

The singular value spectrum for the first 100 modes of the training data from the previous section is presented in Fig. 9, where a similar trend is observed as in Fig. 4, and the total reconstruction error (relative L2-norm evaluated at all spatial and temporal points) is shown as a function of the number of sampling points in Fig. 10. It is seen that the QDEIM constantly results in more accurate reconstructions than the DEIM and the ADEIM generally performs better [a] than the two static methods.

Following the choice in previous section, detailed analysis is conducted on $m_L = 151$ (12.5% of the total number of modes) and the results for $m_L = 31$ (2.6% of the total) are also presented. Two cycles of the signal monitored at the same location as in the previous sections are shown in Fig. 11 along with the L2 error history. In this 1D application, all methods captured the pressure signal to within a few % accuracy, with the QDEIM achieving slightly less error than the DEIM and the ADEIM reconstruction appearing visually superior.

The pressure profile when the error reaches a maximum is also presented in Fig. 12. The ADEIM is seen to locate more sampling points closer to the large gradient in the signal (e.g. at $x = -0.045$m), and results in a more faithfully reproduced profile.

### B. Axisymmetric (2D) results

Similar tests are then performed on high-fidelity (full-order) 2D snapshots of pressure from a simulation of the CVRC.[39] The simulation was performed on a 110,826-node mesh with the GRI 1.2 hydrocarbon reaction mechanism set consisting of 32 chemical species and 177 reactions. Snapshots of the full-order data were recorded every $5\mu s$ and 1025 snapshots are taken in total. In the present study, 700 snapshots are used as training data covering a period of 5 pressure oscillation cycles, and the rest are retained for testing.

The singular value spectrum for the first 100 modes of the training data is presented in Fig. 13, where a larger decay rate than the 1D case is observed, providing the foundation for more sparse reconstructions.

[a] The anomalous result at $m_L = 101$ requires further investigation as the DEIM achieves its minimum error while a peak is observed for ADEIM at the same point. The random selection of the additional sampling points in ADEIM could be at fault.

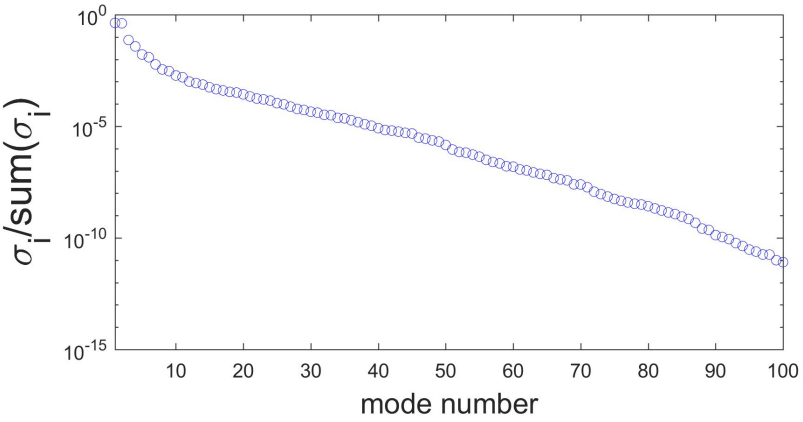


Figure 9: Singular value spectrum for 1D training data

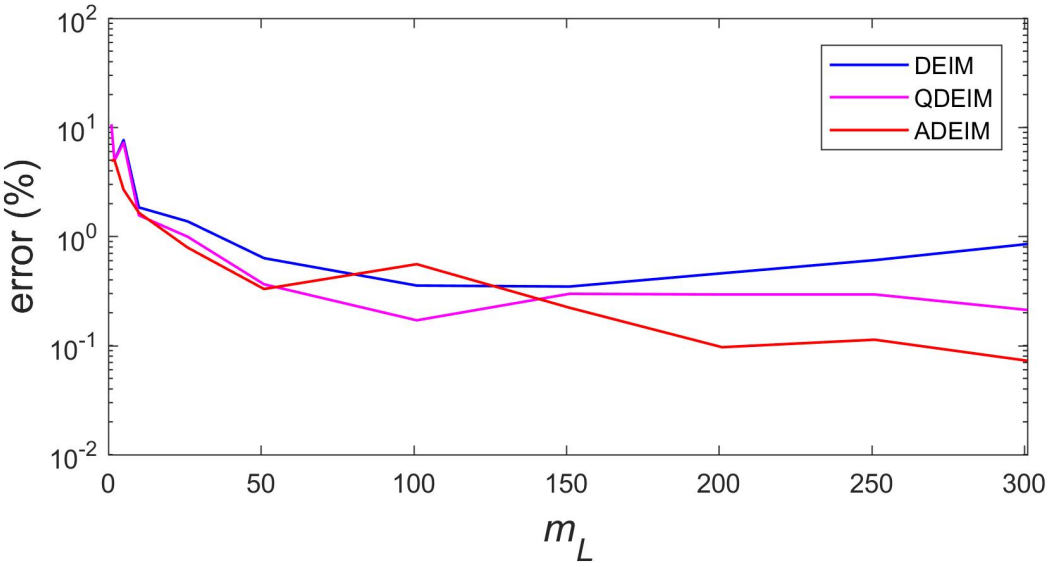


Figure 10: 1D sparse sampling reconstruction error at variate $m_L$

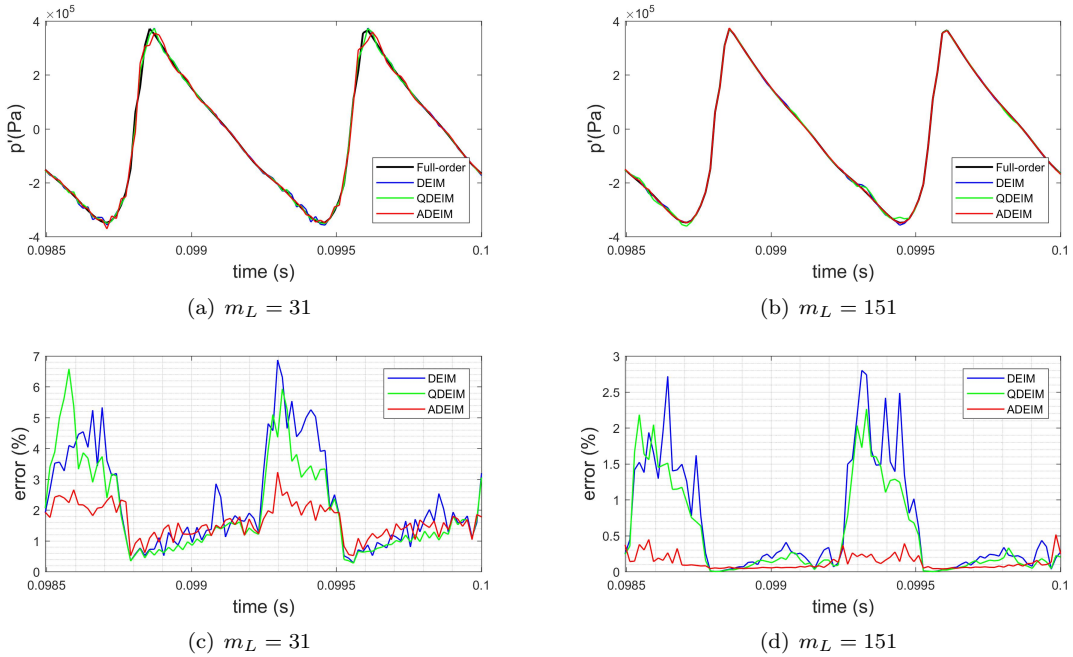


(a) $m_L = 31$ (b) $m_L = 151$

(c) $m_L = 31$ (d) $m_L = 151$

Figure 11: Pressure perturbation signal and error history for 1D sparse sampling reconstruction

Based on the number of available high-fidelity data snapshots, the maximum number of sampling points that were evaluated is 700, corresponding to just 0.63% of the total.

The total reconstruction error (space and time) is plotted against number of sampling points in Fig. 14. The error decays in a similar trend as the singular values, and the ADEIM results in a considerably reduced error than the DEIM in most cases. The QDEIM manages to perform close to the ADEIM in most tests, yet a unexpected deficiency occurs at $m_L = 100$ and requires further investigation.

The reconstruction results using 700 sampling points are shown in Fig. 15, where training data is in $t < 0$ and testing data in $t > 0$. The results indicate that the updated basis plays a more important role in reducing the error.

Despite this observation, no significant differences were observed in the sectionally-averaged pressure history.

Comparisons of detailed error profiles are given in Fig. 16. The average L2 error for all methods are below 3% with ADEIM performing noticeably better. The difference can be better visualized in the $x - t - error$ diagram.

## VII. Conclusions

Working towards a broad vision of developing predictive reduced order models of liquid-fueled rocket engines, this work explored the application of projection-based reduced-order models (ROM) to a single element model rocket combustor. As a representative geometry, the continuous variable resonance combustor (CVRC)[17,18] was investigated. Two types of models were considered: i) Quasi-one-dimensional Euler equations with one additional transport equation and a source term to represent heat release; and ii) Axisymmetric solutions based on 32-species finite rate chemistry.

A projection-based ROM solver was developed for the quasi-1D model. By retaining 12.5% of the full order modes, the ROM was shown to be able to capture the evolution, growth and saturation of pressure perturbations to within 2% accuracy in an L2 sense. This result was verified to be consistent for a range of geometric and heat release parameters.

To further reduce the computational complexity, the viability of using sparse sampling was explored. The discrete empirical interpolation method (DEIM) and two variants, namely QR decomposition-based DEIM (QDEIM) and adaptive DEIM (ADEIM) were introduced. The static methods (DEIM/QDEIM) select the

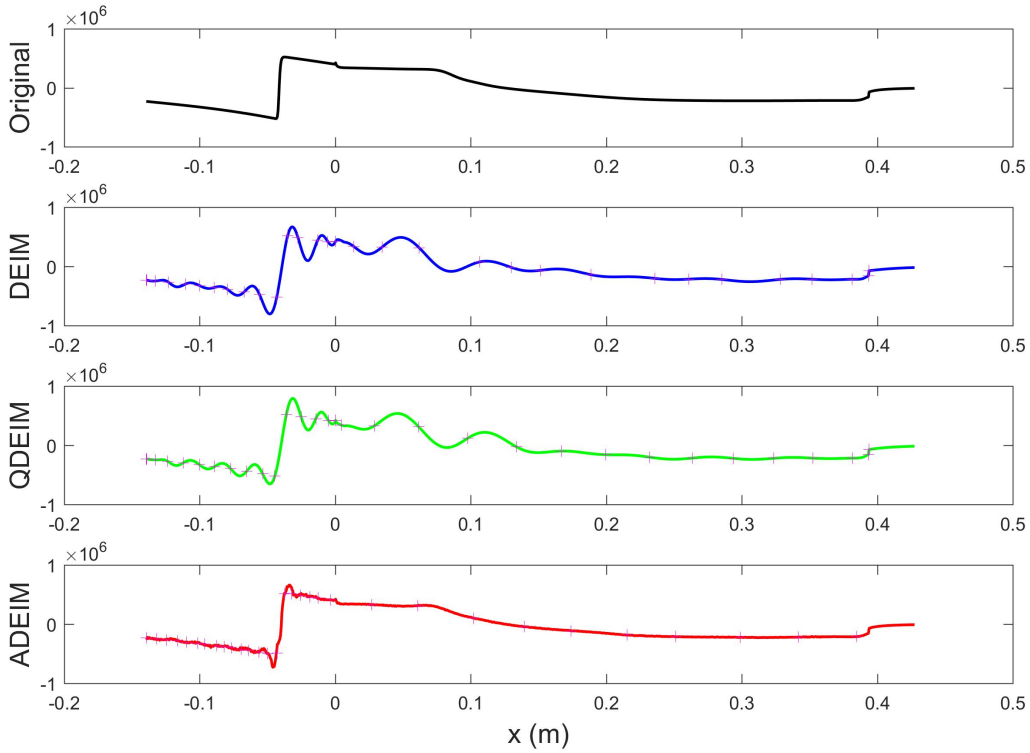


(a) $m_L = 31$

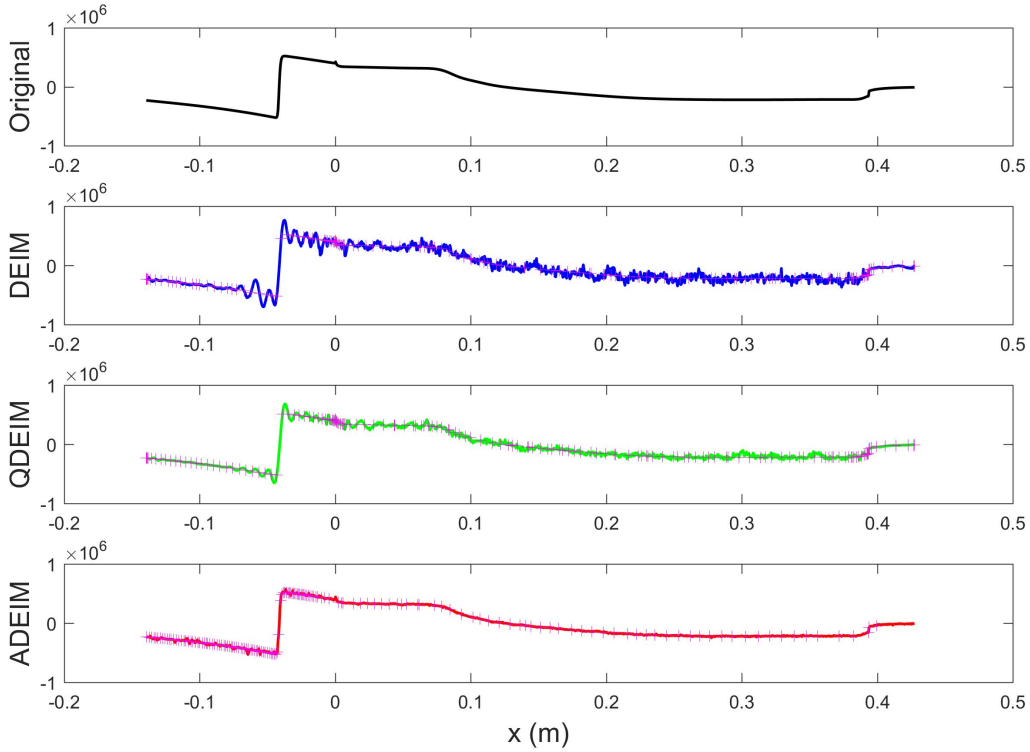


(b) $m_L = 151$

Figure 12: 1D spatial pressure distribution at instant of maximum error. Sampling points marked by magenta crosses.

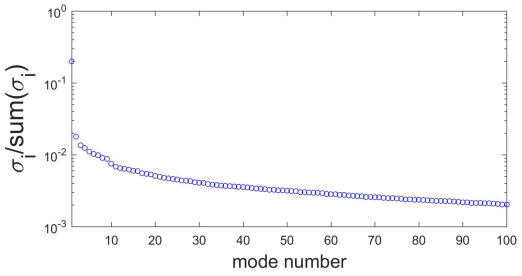


Figure 13: Singular value spectrum for 2D training data

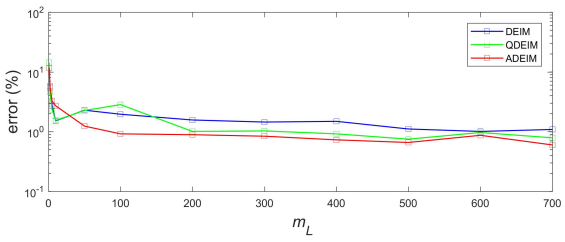


Figure 14: 2D sparse sampling reconstruction error at variate $m_L$



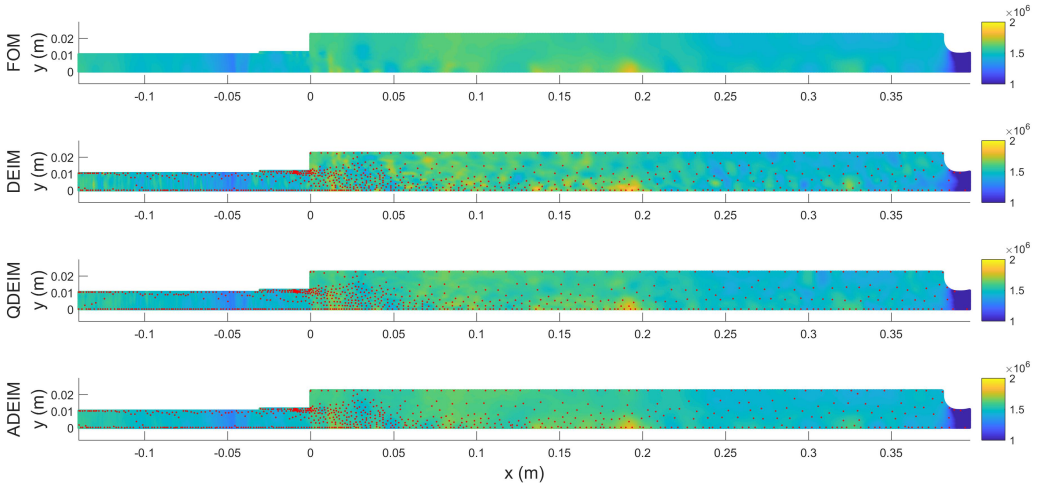


(a) Instantaneous pressure field. Sampling points marked by red dots.

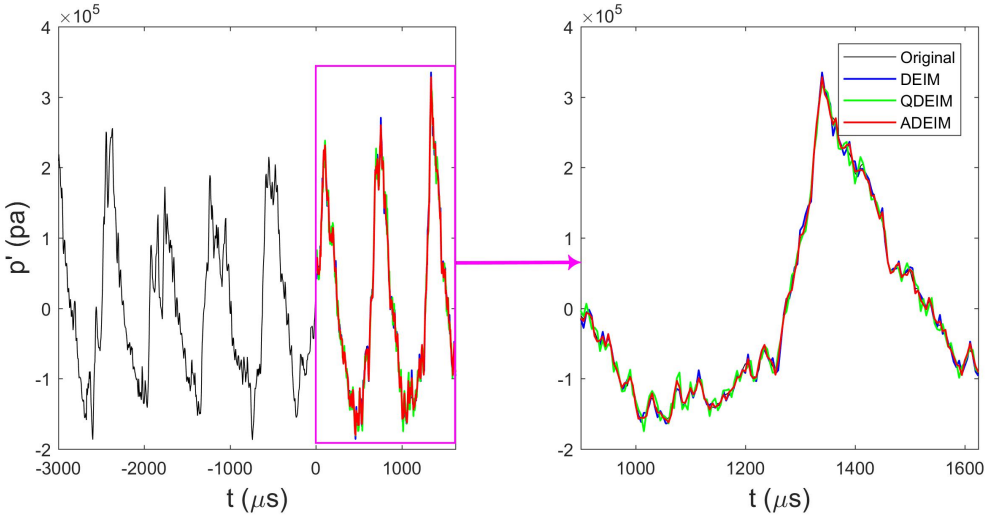


(b) History of average pressure at $x = 0.05$m

Figure 15: 2D sparse sampling reconstruction from 0.63% of total points

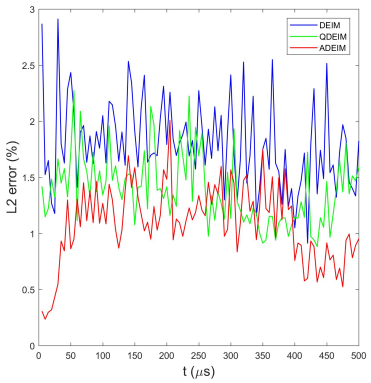


(a) Error history

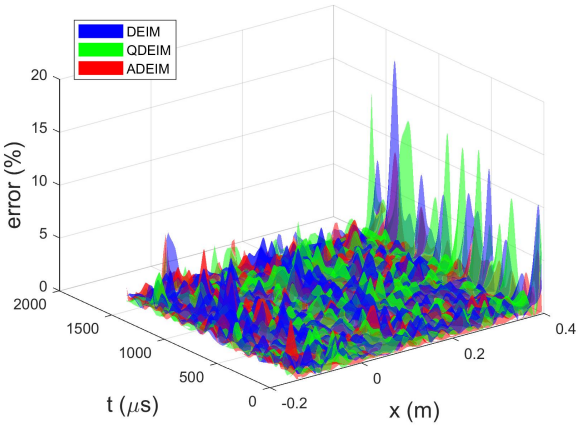


(b) Sectional-temporal error profile

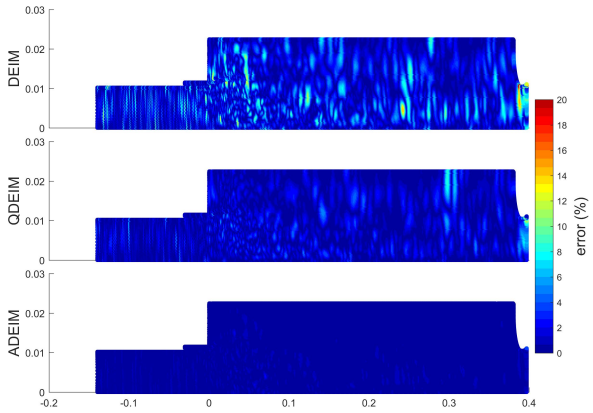


(c) Spatial error distribution, $t = 0\mu s$

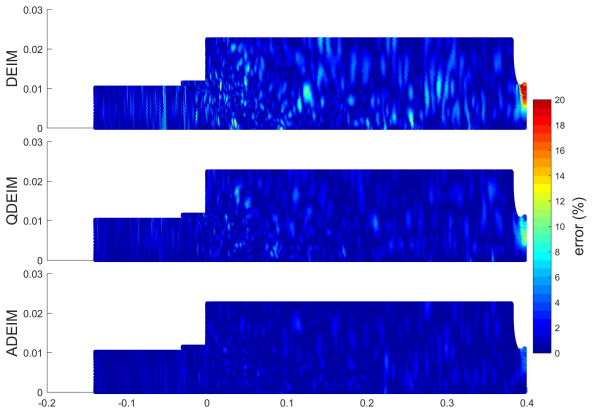


(d) Spatial error distribution, $t = 500\mu s$

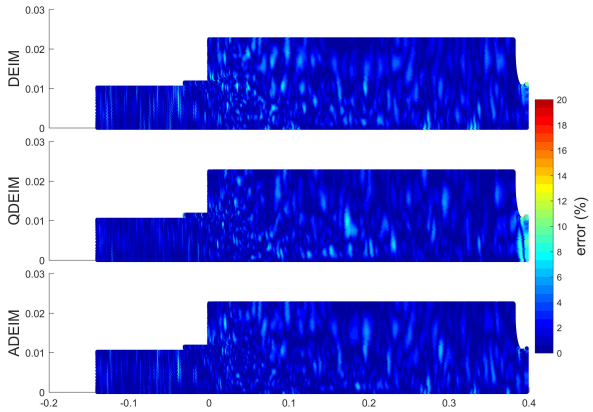


(e) Spatial error distribution, $t = 1000\mu s$

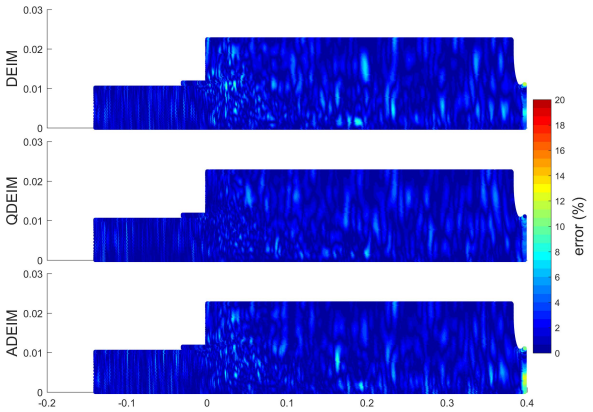


(f) Spatial error distribution, $t = 1500\mu s$

Figure 16: Error in 2D sparse sampling reconstruction from 0.63% of total points

sensors by minimizing the sampling error for a fixed basis. The ADEIM is an online method that updates the basis as well as sampling points by taking randomly picked auxiliary evaluation points at each step and minimizing interpolation errors.

Predictive sampling/reconstruction tests were performed on data from the quasi-1D solver as well as axisymmetric (2D) simulations.[39] In the 1D test, the pressure was reconstructed in the entire domain using 12.5% of the points. The static methods achieved a reconstruction error below 3% and ADEIM further reduced the error to below 0.5%. In the 2D case, pressure reconstruction was performed from 0.63% of the total points, resulting in errors of 3%, 2.5% and 2% using the DEIM, QDEIM and ADEIM, respectively. It is notable that the reconstruction evaluations were performed on data that was not used in the formulation of the sample selection basis functions.

The ability of the ADEIM to adapt the sampling points and basis functions to the state of flow was shown to result in consistently improved reconstructions compared to static methods.

An interesting observation in the 2D problem was that no significant differences were observed between the reconstructions from the three methods when sectionally averaged quantities were considered. This could potentially imply that the prediction of system level quantities might be less sensitive to the sparse sampling scheme.

This work suggests that the ADEIM might prove to be a viable approach for application in predictive ROMs of realistic rocket combustors. reconstruction of localized quantities such as species mass fractions have to be assessed as they may pose a different set of challenges compared to a more global quantity such as pressure. Further, it has to be mentioned that the ADEIM involves additional cost from the minimization problem which has to be solved at every (or every few) time step(s).



## Acknowledgement

The authors thank Prof. Benjamin Peherstorfer for providing help in implementing the ADEIM method as well as Dr. Swanand Sardeshmukh and Dr. Cheng Huang for providing high-fidelity simulation data. This work was supported by AFOSR grant FA9550-17-1-0195 titled *Multi-Fidelity Modeling of Rocket Combustor Dynamics*.

## References

[1]Richardson, E., Skinner, T., Blackwood, J., Hays, M., Bangham, M., and Jackson, A., "An Experimental Study of Unconfined Hydrogen/Oxygen and Hydrogen/Air Explosions," 2014.

[2]Harper, B., Ellison, L. R., and Moser, M. D., "Combustion Instability Analysis and the Effects of Drop Size on Acoustic Driving Rocket Flow," 2004.

[3]Harvazinski, M. E., Huang, C., Sankaran, V., Feldman, T. W., Anderson, W. E., Merkle, C. L., and Talley, D. G., "Coupling between hydrodynamics, acoustics, and heat release in a self-excited unstable combustor," *Physics of Fluids (1994-present)*, Vol. 27, No. 4, 2015, pp. 045102.

[4]Grad, H., "Resonance burning in rocket motors," *Communications on Pure and Applied Mathematics*, Vol. 2, No. 1, 1949, pp. 79–102.

[5]Summerfield, M., "A theory of unstable combustion in liquid propellant rocket systems," *Journal of the American Rocket Society*, Vol. 21, No. 5, 1951, pp. 108–114.

[6]Hart, R. and McClure, F. T., "Theory of acoustic instability in solid-propellant rocket combustion," *Symposium (International) on Combustion*, Vol. 10, Elsevier, 1965, pp. 1047–1065.

[7]Culick, F. E. and Yang, V., "Overview of combustion instabilities in liquid-propellant rocket engines," *Liquid Rocket Engine Combustion Instability*, Vol. 169, 1995, pp. 3–37.

[8]Domingo, P., Vervisch, L., and Réveillon, J., "DNS analysis of partially premixed combustion in spray and gaseous turbulent flame-bases stabilized in hot air," *Combustion and Flame*, Vol. 140, No. 3, 2005, pp. 172–195.

[9]Ihme, M., Zhang, J., He, G., and Dally, B., "Large-eddy simulation of a jet-in-hot-coflow burner operating in the oxygen-diluted combustion regime," *Flow, turbulence and combustion*, 2012, pp. 1–16.

[10]Huang, C., Yoon, C., Gejji, R. M., Anderson, W., and Sankaran, V., "Computational study of combustion dynamics in a single-element lean direct injection gas turbine combustor," *52nd Aerospace Sciences Meeting*, 2014, p. 0620.

[11]Baukal Jr, C. E., Gershtein, V., and Li, X. J., *Computational fluid dynamics in industrial combustion*, CRC press, 2000.

[12]Harvazinski, M. E., *Modeling self-excited combustion instabilities using a combination of two-and three-dimensional simulations*, Ph.D. thesis, PURDUE UNIVERSITY, 2012.

[13]Abramzon, B. and Sirignano, W., "Droplet vaporization model for spray combustion calculations," *International journal of heat and mass transfer*, Vol. 32, No. 9, 1989, pp. 1605–1618.

[14]Frezzotti, M. L., Terracciano, A., Nasuti, F., Hester, S., and Anderson, W. E., "Low-order model studies of combustion instabilities in a DVRC combustor," *50th AIAA/ASME/SAE/ASEE Joint Propulsion Conference*, 2014, p. 3485.

[15]Richecoeur, F., Hakim, L., Renaud, A., and Zimmer, L., "DMD algorithms for experimental data processing in combustion," 2012.

[16]Wierman, M., Pomeroy, B., Feldman, T., Hallum, W., and Anderson, W., "Application of proper orthogonal decomposition to light intensity measurements of combustion instability," *48th AIAA/ASME/SAE/ASEE Joint Propulsion Conference & Exhibit*, 2012, p. 4203.

[17]Yu, Y., Sisco, J. C., Rosen, S., Madhav, A., and Anderson, W. E., "Spontaneous longitudinal combustion instability in a continuously-variable resonance combustor," *Journal of Propulsion and Power*, Vol. 28, No. 5, 2012, pp. 876–887.

[18]Yu, Y. C., *Experimental and analytical investigations of longitudinal combustion instability in a continuously variable resonance combustor (CVRC)*, Ph.D. thesis, Purdue University, 2009.

[19]Frezzotti, M. L., Nasuti, F., Huang, C., Merkle, C., and Anderson, W. E., "Response Function Modeling in the Study of Longitudinal Combustion Instability by a Quasi-1D Eulerian Solver," *51st AIAA/SAE/ASEE Joint Propulsion Conference*, 2015, p. 3840.

[20]Frezzotti, M. L., Nasuti, F., Huang, C., Merkle, C., and Anderson, W. E., "Parametric Analysis of Response Function in Modeling Combustion Instability by a Quasi-1D Solver," *6th EUROPEAN CONFERENCE FOR AEROSPACE SCIENCES*, 2015.

[21]Hutzel, J. R., Decker, D. D., and Donbar, J. M., "Scramjet isolator shock-train leading-edge location modeling," *17th AIAA International Space Planes and Hypersonic Systems and Technologies Conference*, 2011, pp. 1–15.

[22]MacMartin, D. G., "Dynamics and control of shock motion in a near-isentropic inlet," *Journal of aircraft*, Vol. 41, No. 4, 2004, pp. 846–853.

[23]Mayer, D. W. and Paynter, G. C., "Prediction of supersonic inlet unstart caused by freestream disturbances," *AIAA journal*, Vol. 33, No. 2, 1995, pp. 266–275.

[24]Noack, B. R., Schlegel, M., Morzynski, M., and Tadmor, G., "Galerkin method for nonlinear dynamics," *Reduced-Order Modelling for Flow Control*, Springer, 2011, pp. 111–149.

[25]Carlberg, K., Farhat, C., Cortial, J., and Amsallem, D., "The GNAT method for nonlinear model reduction: effective implementation and application to computational fluid dynamics and turbulent flows," *Journal of Computational Physics*, Vol. 242, 2013, pp. 623–647.

[26]Lucia, D. J., King, P. I., and Beran, P. S., "Reduced order modeling of a two-dimensional flow with moving shocks," *Computers & Fluids*, Vol. 32, No. 7, 2003, pp. 917–938.

[27]Yamaleev, N. K. and Pathak, K. A., "Nonlinear model reduction for unsteady discontinuous flows," *Journal of Computational Physics*, Vol. 245, 2013, pp. 1–13.

[28]Marley, C. D., Duraisamy, K., and Driscoll, J. F., "Reduced Order Modeling of Compressible Flows with Unsteady Normal Shock Motion," *51st AIAA/SAE/ASEE Joint Propulsion Conference*, 2015, p. 3988.

[29]Kutz, J. N., *Data-driven modeling & scientific computation: methods for complex systems & big data*, OUP Oxford, 2013.

[30]Chaturantabut, S. and Sorensen, D. C., "Discrete empirical interpolation for nonlinear model reduction," *Decision and Control, 2009 held jointly with the 2009 28th Chinese Control Conference. CDC/CCC 2009. Proceedings of the 48th IEEE Conference on*, IEEE, 2009, pp. 4316–4321.

[31]Chaturantabut, S. and Sorensen, D. C., "Nonlinear model reduction via discrete empirical interpolation," *SIAM Journal on Scientific Computing*, Vol. 32, No. 5, 2010, pp. 2737–2764.

[32]Drmac, Z. and Gugercin, S., "A new selection operator for the discrete empirical interpolation method—Improved a priori error bound and extensions," *SIAM Journal on Scientific Computing*, Vol. 38, No. 2, 2016, pp. A631–A648.

[33]Drmač, Z. and Saibaba, A. K., "The Discrete Empirical Interpolation Method: Canonical Structure and Formulation in Weighted Inner Product Spaces," *arXiv preprint arXiv:1704.06606*, 2017.

[34]Chan, T. F., "Rank revealing QR factorizations," *Linear algebra and its applications*, Vol. 88, 1987, pp. 67–82.

[35]Chan, T. F. and Hansen, P. C., "Low-rank revealing QR factorizations," *Numerical Linear Algebra with Applications*, Vol. 1, No. 1, 1994, pp. 33–44.

[36]Gu, M. and Eisenstat, S. C., "Efficient algorithms for computing a strong rank-revealing QR factorization," *SIAM Journal on Scientific Computing*, Vol. 17, No. 4, 1996, pp. 848–869.

[37]Mojgani, R. and Balajewicz, M., "Lagrangian basis method for dimensionality reduction of convection dominated nonlinear flows," *arXiv preprint arXiv:1701.04343*, 2017.

[38]Peherstorfer, B. and Willcox, K., "Online adaptive model reduction for nonlinear systems via low-rank updates," *SIAM Journal on Scientific Computing*, Vol. 37, No. 4, 2015, pp. A2123–A2150.

[39]Sardeshmukh, S. V., Heister, S. D., and Anderson, W. E., "Prediction of Combustion Instability with Detailed Chemical Kinetics," *53rd AIAA Aerospace Sciences Meeting*, 2015, p. 1826.